Real-Time Modeling of Agile Fixed-Wing UAV Aerodynamics

Waqas Khan, and Meyer Nahon, *Senior Member, IEEE*

Abstract— **Agile UAVs is a special class of fixed-wing aircraft characterized by high thrust-to-weight ratios (around 2 to 3) and big control surfaces (around 40 to 50% chord) with deflections as large as 50 degrees; and hence capable of extreme maneuvers and aerobatics. The intent of this paper is to model the aerodynamics of agile UAVs for real-time applications such as pilot-in-loop aircraft simulation, accounting for the unique geometry of the aerodynamic/ control surfaces, high angles of attack encountered during maneuvers and aerobatics, and also unforeseen changes in the aerodynamics in the event of a crash/ accident. Conventional modeling techniques, such as the stability derivatives approach, are not suitable due to the highly nonlinear nature of the aerodynamics and in particular because of the strong coupling of the aircraft states. Hence in the present work, a component breakdown approach is utilized to model agile UAV aerodynamics for the complete angle of attack range. Simplifications have made in the model to retain real-time functionality without losing much accuracy. For the purpose of validation, wind-tunnel testing is done for different angle of attack conditions including completely reversed flow. A good agreement between the simulation and experiments establishes the validity of the proposed approach and the aerodynamics model, with max. rms errors of ~0.15 N and 0.05 N.m in aerodynamic forces and moments.**

I. INTRODUCTION

The wide variety of UAVs available today can be broadly classified into either fixed-wing (conventional) UAVs or rotary-wing UAVs (such as helicopters and quadcopters). The former type has traditionally been associated with conventional cruise flight, and only the later type has been assumed to have maneuvering capabilities. This is no longer true with the recent emergence of a special class of fixed-wing UAVs called agile UAVs that, with their low weight, control surfaces as big as 50% chord, large deflections of over 50 degrees, and powerful thrusters producing high thrust-to-weight ratio of ~2 and a strong slipstream, attain maneuverability paralleling that of rotary-wing UAVs, while retaining their capability of long distance cruise flight, see Fig. 1. As such, agile UAVs are suitable for a wide range of tasks such as conventional flight, V/STOL, hovering, perching, rapid evasive maneuvering etc.

Agile UAVs have reignited interest in fixed-wing UAVs as many researchers are now determined to automate their unconventional capabilities [1-3]. Among the several challenges that this task pose, the main one is to model the

Waqas Khan is a Ph.D. candidate in the Dept. of Mechanical Engineering, McGill University, Montreal, QC, Canada. (phone: +1 514-560-3637; e-mail: waqas.khan@mail.mcgill.ca).

Meyer Nahon is a Professor in the Dept. of Mechanical Engineering, McGill University, Montreal, QC, Canada (e-mail: meyer.nahon@mcgill.ca).

Fig. 1. An agile fixed-wing UAV performing aerobatics that involve high angles of attack aerodynamics.

aircraft aerodynamics for the complete ±180 degree angle of attack range, in addition to catering for the large deflections of their big control surfaces. Many works in the literature employ system identification techniques that rely on experimentally obtained data to identify transfer functions from the control inputs (aileron, elevator and rudder commands) to the roll, pitch and yaw rates of the aircraft. The experimental data may be obtained from extensive flight tests [4, 5], wind-tunnel [6], and even using motion tracking [7-9]. Although this eliminates the need of evaluating the complex aerodynamic forces and other nonlinear effects at high angles of attack, the downside is that the identified model has no physical basis, and exhaustive testing must be carried out before the model can even come close to covering the full flight envelope. Hence system ID technique may well be used only for specific cases and not to cover the entire flight envelope. Some works in the literature that deal with specific maneuvers like hovering etc. of agile UAVs, use stability derivatives to model the aerodynamics [10-12]. Application of stability derivatives to agile UAVs requires linearization of their nonlinear dynamics model about the desired maneuver conditions, and will lead to more-than-one linear models. For example, [10] presents two independent models – one linearized about level flight conditions and the other about hover condition. Aerodynamic forces in each model are calculated using stability derivatives. The problem, besides having to deal with multiple models, is to devise a control strategy to intelligently switch between models. Again, this may be feasible only for a few maneuvers and not for the entire flight envelope.

Another approach used quite often in the literature is the component breakdown approach [13, 14]. In this approach, the components of the aircraft such as the wing, tail, fuselage etc., are divided into a number of segments, each producing lift, drag and moment about its own aerodynamic center. These forces and moments are transferred to the aircraft's center of gravity (c.g.) using kinematics, and summed up to
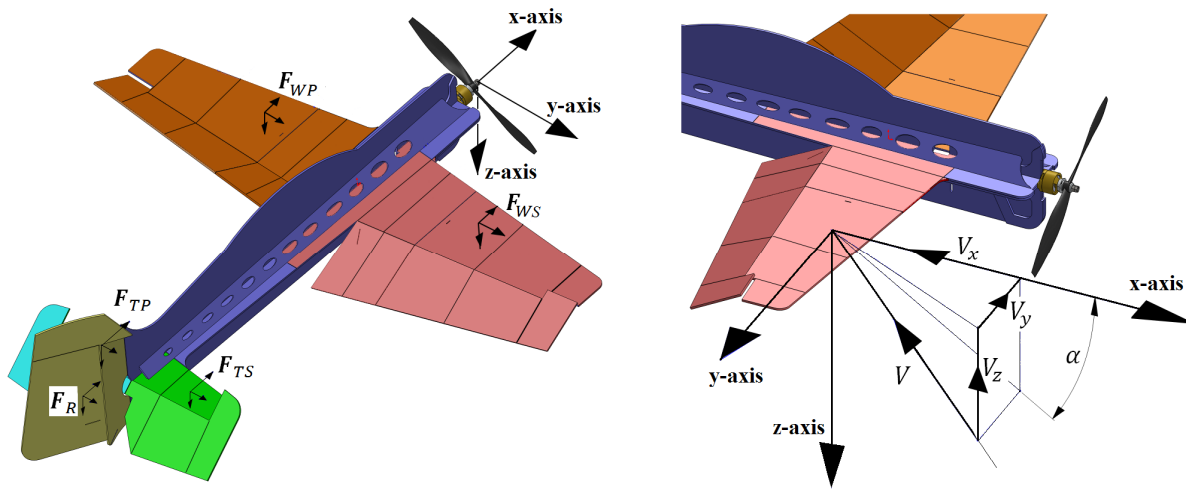
Fig. 2. (Left) A fixed-wing UAV divided into segments for the component breakdown approach. Aerodynamic forces on a few segments are also shown. The standard aircraft frame is placed at the nose of the aircraft. (Right) Velocity and angle of attack experienced locally by one segment of the starboard wing.

give the total aerodynamic forces and moments. The benefit of this approach for agile UAVs is that 1) it can handle the unusual geometry of the aircraft surfaces for e.g. the elevator in Fig. 1, and 2) it can model partially stalled surfaces like the part of the wing immersed in the propeller slipstream that stalls later than the rest of the wing [15]. The outcome of this approach is a single unified model that, by design, also considers realistic phenomenon such as adverse yaw, induced roll etc. Aerodynamic database covering the full angle of attack range, i.e. $-180^{\circ} \leq \alpha \leq 180^{\circ}$, is needed for each segment to determine the aerodynamic forces and moments acting on it. Such a database can be constructed in a number of ways; for example, Kubo [16] combines up-to-stall NACA4412 data with 180 degree NACA0012 data to generate full angle of attack aerodynamic curves for 2D lift coefficient C_l, drag coefficient C_d and moment coefficient C_m. Wind-tunnel testing has also been undertaken by Kubo in a later work [6] for the same purpose. In Ref. [13], C_l, C_d and C_m curves are modeled in parametric form using nonlinear lifting line theory over the complete angle of attack range. Post-stall aerodynamics is modeled like a flat plate producing only form drag. A weighting function is used to transition smoothly from streamline aerodynamics ($\alpha \leq 30^{\circ}$) to bluff body aerodynamics. A more accurate approach to generate ±180 degree aerodynamic data is described in [14]. Available experimental data is used together with XFOIL [17] at low angles of attack, and semi-empirical methods at high angles of attack. In all the aforementioned works, the aerodynamics are pre-evaluated either using theoretical methods or using wind-tunnel experiments, and stored in huge lookup tables for use in real-time applications. This method is probably not efficient as any minor change in the aircraft's configuration as a result of a design iteration or damage to the aerodynamic surfaces in the event of a crash etc., will require re-evaluation of the lookup tables that may not be possible in real-time.

In the current work, a theoretical method for modeling full envelope aerodynamics capable of running in real-time is

presented. Real-time execution of a simulation implies that the model equations must be solvable on the target computer at the desired rate. In the present work, we aim for execution of the simulation code at a rate of ~100 Hz on a standard desktop PC. The presented model accounts for pre-stall and post-stall aerodynamics, as well as the effect of aspect ratio, and big control surfaces with large deflections. It requires few inputs and is non-iterative, making it feasible for real-time applications such as pilot-in-loop simulation. The component breakdown approach along with the presented aerodynamics model is validated via wind-tunnel experiments. In the next section, the component breakdown method is discussed followed by the aerodynamics model in Section III. Validation is presented in Section IV and conclusions in Section V.

II. COMPONENT BREAKDOWN APPROACH

It is first useful to discuss the component breakdown approach before modeling aerodynamics of agile UAVs. As alluded earlier, this approach allows us to model each segment independently with its own aerodynamics, and the possibility of modeling almost every detail of the aircraft. This means, for example, that some segments can be modeled with different velocity due to the propwash over them; some segments may be modeled as 100% control surfaces while others can be partial control surfaces etc.

Fig. 2 shows the component breakdown approach applied to *YAK 54* – a high performance RC model aircraft. The segments are defined keeping in view the aircraft geometry and other constraints like propwash etc. In Fig. 2, the starboard wing is divided into six segments, such that the first three segments (from the fuselage) lie within the propeller slipstream. More so, the first segment at the wing root has no control surface, while the last segment at the tip has a different configuration with an aileron horn. Likewise, segments can be defined for all components of the aircraft. Then depending on the condition and geometry of each segment, it will produce its own aerodynamic forces and moments.

1189

III. Aerodynamics Modeling

In this section we present a simple model for the aerodynamics of an individual segment, which involves modeling both pre-stall and post-stall aerodynamics, taking into account the effect of aspect ratio, big control surfaces and large deflections.

A. Reference Velocity

Each segment of the aircraft moves with a different velocity which can be obtained from the aircraft's velocity $[u, v, w]^T$ and body rates $[p, q, r]^T$ using kinematics.

$$V_x = u + z_i q - y_i r + V_{p,\text{axial}} + V_{\text{wind},x}$$
$$V_y = v + x_i r - z_i p + V_{\text{wind},y} \qquad (1)$$
$$V_z = w + y_i p - x_i q + V_{p,\text{swirl}} + V_{\text{wind},z}$$

where (x_i, y_i, z_i) is the position of the reference point of the ith segment (taken to be its aerodynamic center) measured from the aircraft c.g., and $V_{p,\text{axial}}$ and $V_{p,\text{swirl}}$ are the axial and swirl components of the propwash measured at the reference point. The propwash velocity may be determined from the classical momentum theory [18] or more accurately using [19]. External wind velocity V_{wind} (measured in the aircraft body frame) is also added vectorially in Eq. (1).

B. Angle of Attack

From Fig. 2, the angle of attack for each segment is

$$\alpha = \tan^{-1}\left(V_z / V_x\right) \qquad (2)$$

for horizontal surfaces like the wing shown in Fig. 2. Conventionally a side slip angle is defined in addition to the angle of attack to fully characterize the motion; but this leads to strong coupling of the lateral and longitudinal dynamics, especially during high angle of attack maneuvers. Therefore, rather than using the side slip angle, researchers like Selig [14] define the angle of attack for the vertical surfaces as $\tan^{-1}(V_y / V_x)$.

C. Effect of Aspect Ratio

Agile UAVs are designed to keep most of the aerodynamic and control surfaces immersed in the propwash to maintain lift and control under zero/low forward speed flight and even extreme maneuvers, wherein the external flow is large detached from the surfaces. This results in low aspect ratio surfaces that affect the flow over each segment defined along those surfaces.

The effect of aspect ratio on the lift-curve slope is well-known and documented in the literature. In the current work, the expression given in [20] is used for the lift-curve slope of the segment belonging to a finite surface of aspect ratio AR.

$$C_{L\alpha} = C_{l\alpha}\left(\frac{AR}{AR + 2(AR+4)/(AR+2)}\right) \qquad (3)$$

in which $C_{L\alpha}$ is the lift-curve slope of a segment of finite aspect ratio surface while $C_{l\alpha}$ is the 2D lift-curve slope. Other expressions for $C_{L\alpha}$ in the literature agree with Eq. (3) within a few percent [20].

D. Effect of Control Surface Deflection

A control surface deflection is comparable to changing the camber of the airfoil, and shifts the lift curve in the linear range. A positive deflection is defined such that it increases the camber and shifts the lift curve upwards, see Fig. 3. For a segment with control surface deflected through $+\delta_f$, the increment in lift coefficient is written from [20] as,

$$\Delta C_L = C_{L\alpha} \tau \eta \delta_f \qquad (4)$$

where $\tau = 1 - (\theta_f - \sin\theta_f)/\pi$ is the flap effectiveness factor, $\theta_f = \cos^{-1}(2c_f/c - 1)$ with c_f and c being the flap chord and airfoil chord respectively. η is an empirical factor to account for the effects of viscosity and can be found from Ref. [20] against flap deflection.

As said earlier, a segment with a positively deflected control surface will add to its camber reducing the zero-lift angle of attack α_0 which can be found from Fig. 3 to be,

$$\alpha_0 = \alpha_{0(\text{base})} - \Delta C_L / C_{L\alpha} \qquad (5)$$

$\alpha_{0(\text{base})}$ is the zero-lift angle of attack due to the geometric camber and is negative by convention for a positive upward camber. $\Delta C_L / C_{L\alpha}$ is due to the camber induced by the control surface deflection and is positive or negative depending on the sign of δ_f in Eq. (4).

Furthermore, the stall angle of an airfoil with deflected control surface is lower than that for no deflection [20]. Hence the increment in $C_{L\max}$ is lower than ΔC_L depending on the c_f/c ratio. $\Delta C_{L\max}$ can be determined from [20] for a
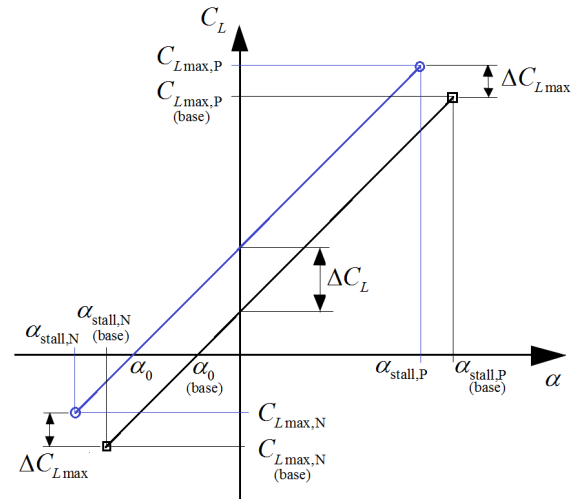

Fig. 3. The effect of control surface deflection on the lift curve in the linear region. The black and blue lines represent no deflection, and positive deflection respectively.

given ΔC_L (from Eq. (4)) and c_f/c ratio. Then the maximum positive and negative lift coefficients are:

$$C_{L\max,P} = C_{L\alpha}\left(\alpha_{stall,P(base)} - \alpha_{0(base)}\right) + \Delta C_{L\max}$$
$$C_{L\max,N} = C_{L\alpha}\left(\alpha_{stall,N(base)} - \alpha_{0(base)}\right) + \Delta C_{L\max} \qquad (6)$$

The corresponding positive and negative stall angles are:

$$\alpha_{stall,P} = \alpha_0 + C_{L\max,P}/C_{L\alpha}$$
$$\alpha_{stall,N} = \alpha_0 + C_{L\max,N}/C_{L\alpha} \qquad (7)$$

E. Low Angle of Attack Aerodynamics

Prior to stalling i.e. $\alpha_{stall,N} \leq \alpha \leq \alpha_{stall,P}$, aerodynamic coefficients are calculated as follows. The lift coefficient is calculated foremost as per Eq. (8) below, and acts at an effective angle of attack α_{eff} since a finite surface induces a downwash reducing the angle of attack by α_i called the induced angle of attack [20]. This induced angle in turn depends on the lift coefficient, and thus iterative methods may be employed to evaluate α_i and C_L for a given angle of attack and control surface deflection. Although iterative methods are accurate, there is no guarantee that the solution will converge within a set time/ number of iterations, which is a critical requirement for real-time simulation. To overcome this problem, it is customary to pre-compute the induced angle (using iterative methods) for a range of angles of attack and control surface deflections, and then to store in lookup tables to be used during real-time application, see for e.g. [14]. A drawback of this approach is that any change in the aircraft configuration then requires re-evaluation of the lookup tables.

In the current work, the iterative process is avoided altogether for the sake of real-time capability by assuming elliptic loading of the aerodynamic surface, so that the induced angle of attack is simply given as per Eq. (8). Some accuracy may be lost but not enough to compel the use of iterative methods. α_i is not considered explicitly in calculating C_L since its effect is already taken into account when using $C_{L\alpha}$ for a finite surface as per Eq. (3). All other aerodynamic coefficients are calculated for α_{eff} according to Eq. (8).

$$C_L = C_{L\alpha}(\alpha - \alpha_0)$$
$$\alpha_i = C_L/(\pi AR)$$
$$\alpha_{eff} = \alpha - \alpha_0 - \alpha_i$$
$$C_T = C_{d,0}\cos\alpha_{eff} \qquad (8)$$
$$C_N = (C_L + C_T\sin\alpha_{eff})/\cos\alpha_{eff}$$
$$C_D = C_N\sin\alpha_{eff} + C_T\cos\alpha_{eff}$$
$$C_M = -C_N\left[0.25 - 0.175(1 - 2\alpha_{eff}/\pi)\right]$$

In the above equations, C_N and C_T are the normal and tangential force coefficients acting normal and along the airfoil, and $C_{d,0}$ is the skin friction coefficient.

F. High Angle of Attack Aerodynamics

It is well known that beyond stall, the profile of an airfoil has negligible effect and thus it acts as a flat plate for which the aerodynamic coefficients may be calculated using flat plate theory [21], or expressions by Hoerner et al. [22], Lindenburg [23], Young et al. [24] or Leishman [25]. In the current work, a combination of these works is used in the high angle of attack region defined by start and end angles $\alpha_{high,S}$ and $\alpha_{high,E}$ respectively. Thus for $\alpha_{high,S} \leq \alpha \leq \alpha_{high,E}$:

$$\alpha_{eff} = \alpha - \alpha_0 - \alpha_i$$
$$C_N = C_{d,90}\sin\alpha_{eff}\left[1/\left(0.56 + 0.44\sin\alpha_{eff}\right)\right.$$
$$\left. -0.41\left(1 - e^{-17/AR}\right)\right]$$
$$C_T = 0.5C_{d,0}\cos\alpha_{eff} \qquad (9)$$
$$C_L = C_N\cos\alpha_{eff} - C_T\sin\alpha_{eff}$$
$$C_D = C_N\sin\alpha_{eff} + C_T\cos\alpha_{eff}$$
$$C_M = -C_N\left[0.25 - 0.175(1 - 2\alpha_{eff}/\pi)\right]$$

Beyond stall, the induced angle of attack α_i is linearly tapered to zero at 90 deg. [14]. As such, in the α_{eff} expression, the induced angle of attack is obtained via linear interpolation between α_i at α_{stall} and $\alpha_i = 0$ at $\alpha = \pm 90^\circ$. $C_{d,90}$ in the above equation represents the 2D drag coefficient of the airfoil normal to the flow.

1) Variation of $C_{d,90}$

The airfoil becomes concave or convex to the flow depending on whether the deflection is positive or negative. Thus the drag coefficient at 90 deg. depends on whether the control surface deflection is positive or negative, as well as the degree of deflection. To account for this variation, Fig. 4.8 of Ref [20] is used, according to which, a 90 deg. concave has a drag coefficient of 2.2, while that for a flat plate is 1.98 and for a 90 deg. convex is 1.55. The segment of an agile UAV may at most form a 50 degree convex or concave to the flow limited by maximum deflection of the control surfaces. Thus the data from [20] is curve fitted to predict $C_{d,90}$ for any lower control surface deflection:

$$C_{d,90} = -4.26\times10^{-2}\delta_f^2 + 2.1\times10^{-1}\delta_f + 1.98 \qquad (10)$$

As an example, for a positive 50 deg. deflection, the airfoil becomes concave and $C_{d,90}$ comes out to be ~2.1, while that for a negative 50 deg. deflection is ~1.8. For zero deflection, $C_{d,90}$ attains the standard value of 1.98 for a flat plate normal to flow.

G. Complete Aerodynamic Curves

For an aircraft segment with known airfoil parameters ($C_{l\alpha}$, $C_{d,0}$, $\alpha_{0(base)}$, $\alpha_{stall,P(base)}$, $\alpha_{stall,N(base)}$, c_f, c, δ_f) and the surface's AR, Eqs. (3)-(10) may be intelligently used to cover the full ±180 deg. angle of attack range.
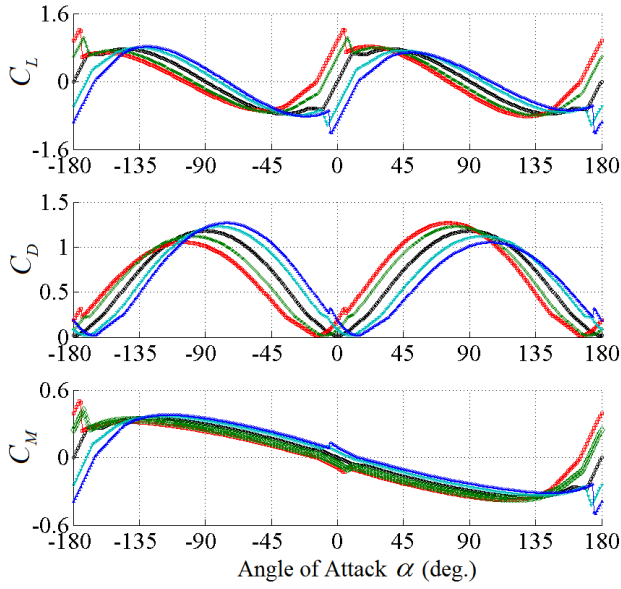
Fig. 4. Complete 180 deg. angle of attack aerodynamic curves for different deflections: 0º (black), +25º (green), +50º (red), -25º (aqua), -50º (blue).

Consider a segment of the agile UAV wing in Fig. 2, with $C_{l\alpha} = 2\pi$, $C_{d,0} = 0.02$, $\alpha_{0(base)} = 0^{o}$, $\alpha_{stall,P(base)} = 10^{o}$, $\alpha_{stall,N(base)} = -10^{o}$, $c_f/c = 0.4$, and $AR = 4$. Full range C_L, C_D and C_M curves are generated for multiple control surface deflections i.e. $\delta_f = 0$, ± 25, and ± 50 degrees. These are plotted in Fig. 4.

Similar aerodynamic curves are presented in [14] that are obtained by combining experimental data and XFOIL at low angles of attack, and semi-empirical equations at high angles of attack. In comparison, the current method is much simpler and implementable in real-time.

IV. VALIDATION

This section deals with the validation of the presented component breakdown approach together with the aerodynamics model.

A. Experimental Setup and Testing Procedure

For preliminary validation, it is deemed best to perform wind-tunnel experiments because the aerodynamic forces/moments can be reliably measured in a controlled environment. Although the intent was to mount the entire aircraft in the wind-tunnel, only the starboard wing of the RC model aircraft *YAK 54* was tested because the available wind-tunnel had a small 2 ft. X 3 ft. test section. The starboard wing validation should suffice for the entire aircraft because all the aerodynamics presented in Section III are validated, and, more importantly, all aerodynamic surfaces of the aircraft (horizontal tail, rudder, fuselage etc.) share similar aerodynamic characteristics i.e. are low AR flat plates with big control surfaces and large deflections.

The starboard wing was fastened to an ATI gamma force/torque (F/T) transducer which measures force and torque in all three directions with a high resolution (0.028 N

in F_x and F_y, 0.056 N in F_z, 0.0014 N.m in torque) and sampling rate of 1000 Hz. The setup is shown in Fig. 5. Wind speeds were measured in the test section using a Reed hot-wire anemometer which has a sampling rate of 1 Hz, and a resolution of 0.01 m/s in the range 0.2-5 m/s, and 0.1 m/s in the range 5.1-25 m/s. An Arduino board was used to send PW signals to a *Hitec HS-65 HB* servo to produce the desired control surface deflections.

Experiments are performed at two wind speeds: 4 m/s and 8 m/s, and three angles of attack: 0, 20 and 180 deg. At a given wind speed and angle of attack, the control surface (in this case the aileron) is deflected from -50 deg. to +50 deg. with 10 deg. steps. Only a few cases at 180 deg. could be tested as the *YAK 54*, made of *depron* foam, bent considerably at that angle of attack.

Post-processing of the F/T data includes 1) removing measurement noise via a third-order zero-phase Butterworth low-pass filter, with a cut-off frequency of 10 Hz, 2) removing the setup drag from the measurements, and 3) transformation of forces and moments from the sensor frame to the aircraft frame placed at its nose (see Fig. 5).

B. Results and Discussion

For simulation, the *YAK 54* starboard wing is divided into 6 segments, such that the first 3 segments lie within the propeller slipstream (radius determined from [19] at this axial distance downstream of the propeller), and the 6th segment covers the part of the wing with a control horn as shown in Fig. 2. For each segment, its mean aerodynamic chord (m.a.c.) is located using standard techniques [20]. Chord c and flap chord c_f are measured on the m.a.c. and the reference point is placed on the m.a.c., $c/4$ distance behind its leading edge. The position of the reference point is measured from the origin of the aircraft frame placed at the nose of the aircraft.

Reference velocities are calculated for all segments using Eq. (1) with $[u,v,w]^T = [p,q,r]^T = 0$, and also setting $V_{p,\text{axial}}$ and $V_{p,\text{swirl}}$ to zero. The wind velocity is calculated from wind-tunnel speed V and angle of attack α as: $V_{\text{wind},x} = V\cos\alpha$, $V_{\text{wind},y} = 0$, and $V_{\text{wind},z} = V\sin\alpha$.
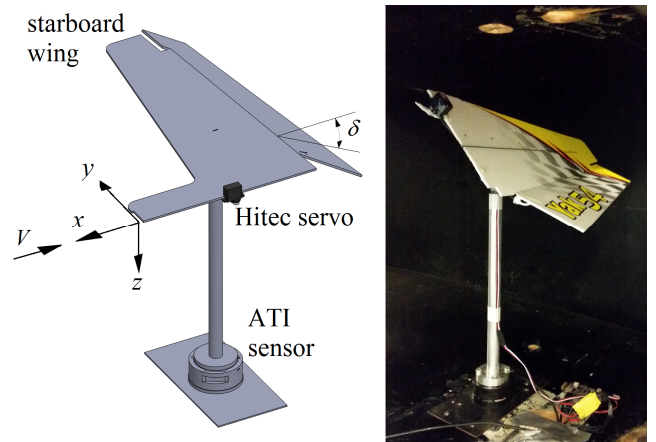

Fig. 5. Experimental setup for the measurement of aerodynamic forces and moments for different wind-speeds, angles of attack, and deflections.

Simulations are run for the test conditions given in the previous section.

1) At Zero Degree Angle of Attack

Fig. 6 shows the simulation results along with experimental data for the zero degree angle of attack case. The force in *y* direction is omitted from the plots because it is zero in both experiments and simulation.

The drag force acting in the $-x$ direction is minimum at zero aileron deflection, and is only due to skin friction. Both positive and negative deflections increase drag, but from experimental measurements, the drag increment for positive deflections is lower than that for corresponding negative deflections. This could be due to the presence of protrusions and structure on the underside of the wing, as well as due to the design-cut spanning the entire length of the underside of the aileron to allow motion. The latter causes flow separation at the wing-aileron joint on negative deflections only, thereby resulting in higher drag. On the contrary, the simulation predicts equal drag increment for positive and negative deflections.

The lift force acts in the $-z$ direction (by standard aeronautical convention) and is zero for no deflection which is expected of a flat plate wing. On positive aileron deflection (introducing a positive camber), an upward lift force ($-F_z$) is generated; while a negative deflection results in a downward force i.e. $+F_z$.

The roll and pitch moments, M_x and M_y, are caused by the lift forces on the segments, that act at reference points located (x_i, y_i, z_i) from the origin of the aircraft frame. For positive deflections, an upward lift force ($-F_z$) will give rise to a negative roll moment about the *x* axis, and a negative pitch moment about the *y* axis. On the other hand, the drag forces on the segments are responsible for the yaw moment M_z; a drag force ($-F_x$) causes a positive M_z.

The overall match between the simulation and experiments is good, with rms errors of 0.06 N in F_x, 0.15 N in F_z, 0.035 N.m in M_x, 0.05 N.m in M_y and 0.02 N.m in M_z.

2) At Other Angles of Attack

Fig. 7 provides the variation of the aerodynamic forces and moments with control surface deflection for different angles of attack. For the completely reversed flow condition i.e. 180 deg. angle of attack, not all deflections could be tested due to severe deformation of the foam wing. More so, the results are shown only for a wind speed of 4 m/s for clarity.

Unlike the 0 deg. angle of attack results, which show symmetry about the zero-deflection value, the 20 degree results are asymmetric. Increment in drag is quite higher for a positive deflection than for the same negative deflection. For a +50 deg. deflection, for e.g., the drag increases to -0.14 N, while for −50 deg. deflection, it increases only to half that value (-0.07 N). Similarly, the lift force variation also becomes asymmetric, increasing by 0.14 N from the zero-deflection value (-0.35 N) at +50 deg. deflection, while reducing twice as much i.e. 0.27 N at -50 deg. deflection.

The roll and pitch moments for the 20 deg. angle of attack follow the asymmetric trend of the lift force discussed above. That is, the change in roll and pitch moments for negative deflections is almost twice that for corresponding positive deflections. The yaw moment follows the same asymmetric trend as that of the drag force, i.e., the change in yaw moment for positive deflections is almost twice of that for corresponding negative deflections.

A standard aircraft wing with starboard and port sides having ailerons that move differentially. It is evident from Fig. 7, that at 0 deg. angle of attack, for any aileron deflection, the wing will not produce lift force and yaw moment, because the two sides produce equal and opposite lift forces and yaw moments that cancel out. However, at 20
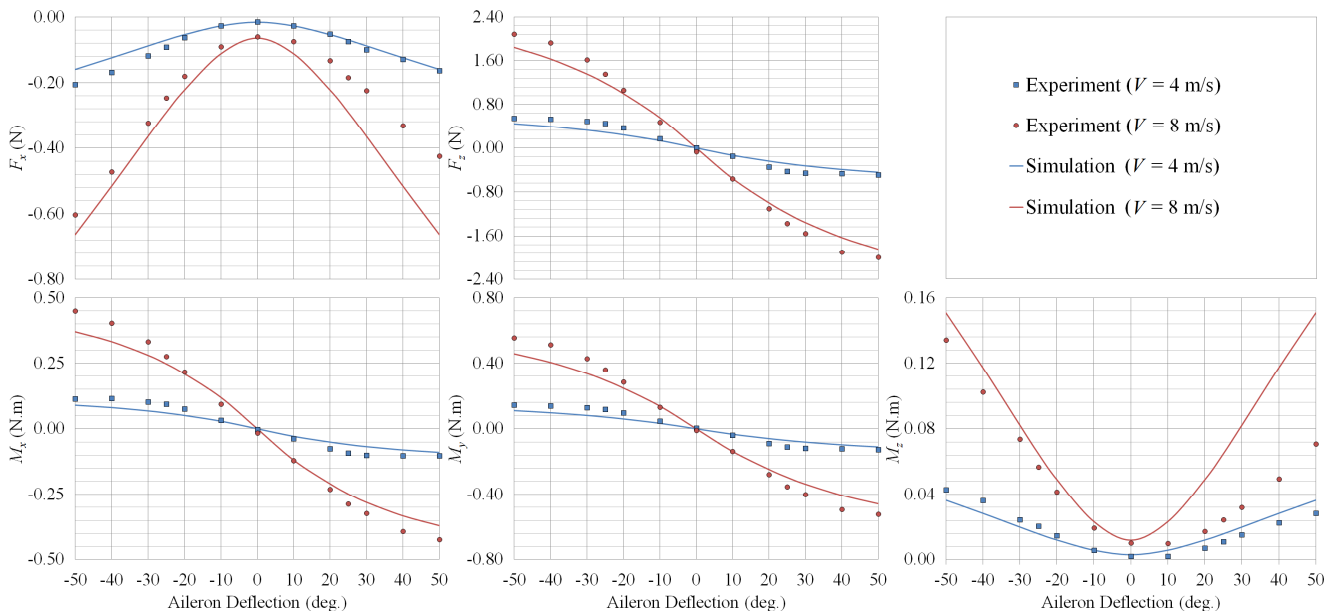

Fig. 6. Simulation versus experimental measurements for the aerodynamic forces and moments at 0 deg. angle of attack and multiple control surface deflections.
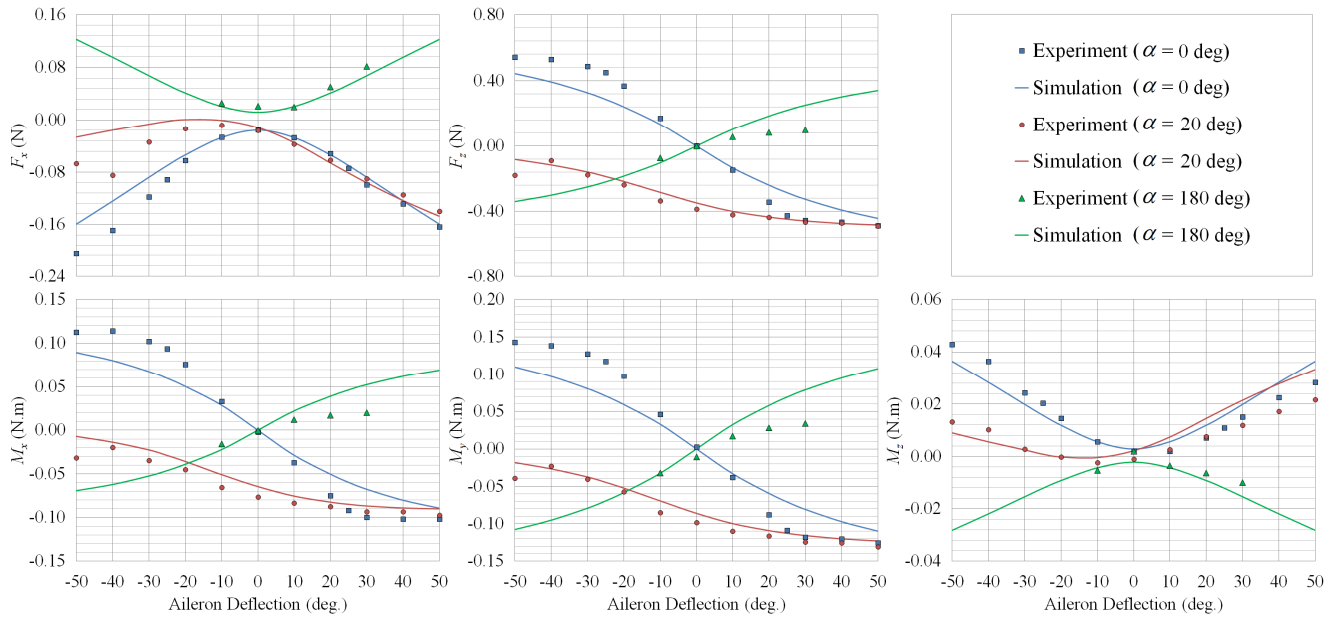
1193

Fig. 7. Simulation versus experimental measurements for the aerodynamic forces and moments at various angles of attack and multiple control surface deflections.

deg. angle of attack and aileron deflection of say +30 deg. (i.e. starboard = +30 deg. and port = -30 deg.), the wing will also produce lift force and yaw moment since the two sides produce opposite but unequal lift forces and yaw moments that do not cancel each other completely. Hence at angles of attack other than 0 deg., the asymmetric variation about the zero-deflection value gives rise to realistic phenomena such as adverse yaw of the ailerons, or induced roll of the rudder etc.

It may also be noted from Fig. 7 that for the 180 deg. angle of attack, all the forces and moments are reversed compared to the 0 deg. case; the drag force acts in the $+x$ direction, while a positive deflection produce a downward force. As expected, the variation of the forces and moments is symmetric about the zero-deflection value.

Overall, the simulation results show a good match with experimental data at both 20 deg. and 180 deg. angles of attack. The rms errors in F_x, F_z, M_x, M_y and M_z are approx. 0.02 N, 0.03 N, 0.01 N.m, 0.01 N.m, and 0.006 N.m respectively for 20 deg. angle of attack, and 0.009 N, 0.08 N, 0.02 N.m, 0.02 N.m, and 0.003 N.m respectively for the 180 deg. angle of attack.

V. CONCLUSION

This paper presents a component breakdown approach to modeling full ±180 deg. aerodynamics of agile UAVs accounting for their low aspect ratios, big control surfaces and large deflections. Since an agile UAV is likely to experience high angles of attack during maneuvers, the aerodynamics model deals with both low angle of attack as well as high angle of attack aerodynamics. The model relies only on simple airfoil parameters: the lift-curve slope, skin friction coefficient, zero-lift angle of attack, and positive and negative stall angles, which are easily available today for any airfoil. The proposed approach also guarantees the

prediction of realistic phenomenon such as induced roll, adverse yaw etc. Some simplifications have been made so that the overall approach is non-iterative and feasible for real-time applications such as pilot-in-loop simulations. This avoids pre-computing the look-up tables on change in aircraft configuration.

Wind-tunnel testing has been undertaken to validate the component breakdown approach in general and the aerodynamics model in particular. Testing is done at different angles of attack including 180 deg. representing completely reversed flow. A very good match is seen between the simulation results and experimental data at all angles of attack and both wind speeds. It is also demonstrated through validation that simplifications made in the aerodynamics model do not result in much loss of accuracy.

REFERENCES

[1] M. F. Sobolic, "Agile Flight Control Techniques for a Fixed-Wing Aircraft," M.S. thesis, Dept. of Aeronautics and Astronautics, Massachusetts Institute of Technology, MA, USA, 2009.

[2] K. J. Krogh, "Developing a Framework for Control of Agile Aircraft Platforms in Autonomous Hover," M.S. Thesis, Dept. of Aeronautics and Astronautics, University of Washington, WA, USA, 2009.

[3] H. D. Blauwe, S. Bayraktar, E. Feron, and F. Lokumcu, "Flight Modeling and Experimental Autonomous Hover Control of a Fixed Wing Mini-UAV at High Angle of Attack," presented at the AIAA Guidance, Navigation and Control Conference and Exhibit, SC, Aug. 20-23, 2007, Paper AIAA 2007-6818.

[4] B. Johnson, and R. Lind, "High Angle-of-Attack Flight Dynamics of Small UAVs," presented at the 47th AIAA Aerospace Sciences Meeting Including The New Horizons Forum and Aerospace Exposition, Orlando, FL, Jan. 5-8, 2009, Paper AIAA 2009-61.

[5] H. Wu, D. Sun, and Z. Zhou, "Model Identification of a Micro Air Vehicle in Loitering Flight Based on Attitude Performance Evaluation," *IEEE Trans. Robotics*, vol. 20, no. 4, pp. 702-712, Aug. 2004.

[6] D. Kubo, K. Maraoka, and N. Okada, "High Angle of Attack Flight Characteristics of a Wing-In-Propeller-Slipstream Aircraft," presented

at the 27th Int. Congress of the Aeronautical Sciences, Nice, France, Sept. 2010.

[7] R. Cory, and R. Tedrake, "Experiments in Fixed-Wing UAV Perching," presented at the AIAA Guidance, Navigation, and Control Conference, Honolulu, Hawaii, Aug. 18-21, 2008, Paper AIAA 2008-7256.

[8] W. Hoburg, and R. Tedrake, "System Identification of Post Stall Aerodynamics for UAV Perching," presented at the AIAA Infotech@Aerospace Conf., Seattle, WA, Apr. 6-9, 2009, Paper AIAA 2009-1930.

[9] D. V. Uhlig, and M. S. Selig, "Determining Aerodynamic Characteristics of a Micro Air Vehicle Using Motion Tracking," *J. Aircraft*, vol. 50, no. 5, pp. 1481-1490, 2013.

[10] W. E. Green, and P. Y. Oh, "A Hybrid MAV for Ingress and Egress of Urban Environments," *IEEE Trans. Robotics*, vol. 25, no. 2, pp. 253-263, 2009.

[11] A. Frank, J. S. McGrew, M. Valenti, D. Levine, and J. P. How, "Hover, Transition, and Level Flight Control Design for a Single-Propeller Indoor Airplane," presented at the AIAA Guidance, Navigation and Control Conference and Exhibit, SC, Aug. 20-23, Paper AIAA 2007-6318.

[12] E. N. Johnson, M. A. Turbe, A. D. Wu, S. K. Kannan, and J. C. Neidhoefer, "Flight Test Results of Autonomous Fixed-Wing UAV Transitions to and from Stationary Hover," presented at the AIAA Guidance, Navigation and Control Conference and Exhibit, Keystone, CO, Aug. 21-24, Paper AIAA 2006-6775.

[13] S. Roy, A. Moreau, and M. Grosbois, "Modeling and Simulation of a Forward-Swept Wing, Vertical Takeoff of Landing & Thrust Vectored Remotely Piloted Vehicle," presented at the 2007 Canadian Aeronautics and Space Institute Annual General Meeting on Aircraft Design and Development Symposium, Toronto, ON, Canada.

[14] M. S. Selig, "Real-Time Flight Simulation of Highly Maneuverable Unmanned Aerial Vehicles," *J. Aircraft*, vol. 51, no. 6, pp. 1705-1725, Nov. 2014.

[15] F. M. Catalano, "On the Effects of an Installed Propeller Slipstream on Wing Aerodynamic Characteristics," *Acta Polytechnica*, vol. 44, no. 3, pp. 8-14, 2004.

[16] D. Kubo, and S. Suzuki, "Tail-Sitter Vertical Takeoff and Landing Unmanned Aerial Vehicle: Transitional Flight Analysis," *J. Aircraft*, vol. 45, no. 1, pp. 292-297, 2008.

[17] M. Drela, "XFOIL: An Analysis and Design System for Low Reynolds Number Airfoils," in *Low Reynolds Number Aerodynamics*, edited by T. J. Mueller, vol. 54 of *Lecture Notes in Engineering*, New York: Springer-Verlag, June 1989, pp. 1-12.

[18] B. W. McCormick, *Aerodynamics of V/STOL Flight*, New York: Dover, 1999, pp. 96-98.

[19] W. Khan, and M. Nahon, "Development and Validation of a Propeller Slipstream Model for Small Unmanned Aerial Vehicles," *J. Aircraft*, to be published.

[20] B. W. McCormick, *Aerodynamics, Aeronautics, and Flight Mechanics*. 2nd ed., New York: John Wiley & Sons, 1995, ch. 3-4.

[21] J. L. Tangler, "Insight into a Wind Turbine Stall and Post-Stall Aerodynamics," *Wind Energy*, vol. 7, no. 3, pp. 247-260, Sept. 2004.

[22] S. F. Hoerner, and B. Henry V, "Fluid-Dynamic Lift: Practical Information on Aerodynamic and Hydrodynamic Lift," NASA STI/Recon Technical Report A 76, 32167, 1975.

[23] C. Lindenburg, "Stall Coefficients," presented at the 2010 IEA Symposium on the Aerodynamics of Wind Turbines, National Renewable Energy Lab, Golden, CO.

[24] S. Young, and F. Donald, "Blade Section Lift Coefficients for Propellers at Extreme Off-Design Conditions," Hydromechanics Directorate Research and Development Report No. CRDKNSWC/HD-1205-02, Carderock Div., Naval Surface Warfare Center, Maryland, Dec. 1997.

[25] J. G. Leishman, *Principles of Helicopter Aerodynamics*. 2nd ed., Cambridge Aerospace Series, New York: Cambridge University Press, 2006.